# Effects of film thickness and magnetism on the electronic structure of MnO films

Asish K. Kundu,[1,*] Sukanta Barman,[1,2] and Krishnakumar S. R. Menon[1,†]

[1]*Surface Physics and Material Science Division, Saha Institute of Nuclear Physics, HBNI, 1/AF Bidhannagar, Kolkata 700064, India*

[2]*Department of Physics, Raja Peary Mohan College, Uttarpara, Hooghly 712258, India*

We investigate the influence of film thickness and magnetism on the electronic structure of a strongly correlated prototypical system, MnO(001) films epitaxially grown on Ag(001), using angle-resolved photoemission spectroscopy (ARPES) and x-ray photoelectron spectroscopy (XPS) techniques. XPS measurements have confirmed the MnO stoichiometry as well as the layer-by-layer growth mode of the films, while the ARPES measurements have confirmed the high structural quality of the films by the observation of clear band dispersions devoid of any sample charging effects. For lower coverage films, finite-size effects/reduced correlation effects are observed, while from 3 ML coverages, bulklike band structures are formed. Detailed band mapping along $\bar{\Gamma}$-$\bar{X}$ and $\bar{\Gamma}$-$\bar{M}$ directions reveal a relative dispersion between Mn-derived $e_g$ and $t_{2g}$ states up to 1.2 eV, in contrast to previous ARPES results where maximum relative dispersions of $\pm 0.1$ eV were reported, while our results excellently match with the theoretically predicted dispersions. By comparing with theoretical results we show the hybridization between O $2p$ with the Mn $e_g$ states giving rise to the observed dispersions resulting from the highly dispersive nature of the O $2p$ bands. Furthermore, we show that during the paramagnetic (PM) to antiferromagnetic (AFM) transition, the valence band gets narrower with an enhancement of the $^5 e_g$ peak intensity, along with the widening of the energy gap by 200 meV. Theoretically, Terakura *et al.* had predicted the possibility of a similar outcome due to the decrease of the effective $dd$ hopping between the oppositely magnetized cations during the PM to AFM-II transition because of the $dd\sigma$ type interaction, yet the experimental verification was absent in the literature. We believe that the exact same mechanism as predicted by Terakura *et al.* is responsible for the changes seen in the electronic structure during magnetic phase transition and argue that a similar trend can be seen for the prototype materials such as CoO and NiO.

## I. INTRODUCTION

Metal supported oxide thin films offer a possible way out from the charging problems which mainly hamper the study of wide band gap insulators by electron spectroscopy techniques. Oxide thin films prepared on metal surfaces are often shown interesting properties and which differs in a spectacular way from the bulk ones, due to the reduced dimensionality, interfacial hybridization, the dielectric boundary effects, etc. Ultrathin oxide overlayers grown on metal substrate reduce their surface Madelung potential which together with the hybridization effect (between the oxide and the metal), may result in the development of an interfacial mixed density of states, in an energy region which is relevant for various chemical interactions [1]. Hence the conductivity gap for insulating oxide thin films on a metal is expected to be substantially reduced which may lead to the enhancement of various exchange and superexchange interaction strength by reducing the on-site Coulomb interactions ($U$) and the charge transfer energy ($\Delta$). Nowadays transition-metal monoxides (NiO, MnO, CoO, FeO, etc.) have been the subject of much experimental and theoretical interest as they show unusual insulating and magnetic properties. The enhanced catalytic behavior of MnO thin film and direct correlation between exchange bias and interfacial spins [2] boosted researchers to look into the structural and electronic properties of ultrathin MnO.

Recent studies on MnO show that the variety of structural, electronic, and magnetic properties are strongly interdependent [3]. Although MnO has partially filled $3d$ states, it is a well-known antiferromagnetic (AFM) insulator with a band gap of 3.8–4.2 eV and Néel temperature of 122 K. Thus, the simple theory based on the band filling concept fails to explain the insulating properties of MnO. The insulating character of MnO can be well described by the use of Mott-Hubbard theory [4], where the $dd$ intra-atomic Coulomb energy opens up a gap between the filled and empty states in the $3d$ band. Spin-density functional band structure calculations also correctly predict the insulating character of MnO [5–8] in the magnetically ordered phase with a gap as large as 2.2 eV [7,8], although still smaller than the gap of 3.8 to 4.2 eV as measured by photoconductivity experiments [9]. It is well known that the oxides of early transition metal $3d$ elements (Ti, V) are classified in the Mott-Hubbard regime, where the band gaps of magnitude $\sim U$ are formed between the upper and lower Hubbard bands because of $\Delta > U$. So far, photoemission studies have revealed that FeO is in the charge transfer regime [10,11], while VO is certainly in the Mott-Hubbard regime [12]. Therefore, MnO should be located near the boundary between the two regimes since $\Delta$ and $U$ are expected to vary systematically as a function of the atomic number of the transition metal. Fujimori *et al.* [12,13] have used a configuration interaction (CI) cluster model calculation for MnO and have suggested that the charge transfer energy may be about the same magnitude as the Mott-Hubbard gap. Although it has been generally recognized that electron-electron correlation effects are of central importance in explaining the electronic structure of these materials, however, Terakura *et al.* [5]

---

*Present address: International Center for Theoretical Physics (ICTP), I-34014 Trieste, Italy; asishkumar2008@gmail.com

†krishna.menon@saha.ac.in

showed that the insulating character of both MnO and NiO can be explained without appeal to the Mott-insulator mechanism. Their calculation suggests that the band structure is strongly dependent upon the magnetic ordering and insulating nature of MnO and NiO can be realized when the magnetization is allowed to vary in the (111) direction. They have also particularly shown that the narrowing of the $e_g(x^2 - y^2, 3z^2 - r^2)$ state in the AFM phase is a crucial condition for making MnO and NiO insulating as well as for stabilizing the local antiferromagnetism, even in absence of a long-range magnetic order.

Hermsmeier *et al.* [14] have attempted to verify this theoretical prediction and carried out UPS measurements in the paramagnetic (PM) and AFM phases of MnO. Their result shows that for the AFM state, the UPS spectra move towards the Fermi level by 300 meV and gets broader than the PM state, while the theoretical prediction made by Terakura *et al.* [5] is just the opposite to these results. Furthermore, an angle-resolved PES study on a single crystal MnO(001) surface [15] suggested that in the valence band, the Mn-derived ($e_g$ and $t_{2g}$) states are separated by 1.8 eV and does not disperse by more than 0.1 eV with respect to each other across the entire Brillouin zone, while theoretical calculations show that the relative dispersion between $e_g$ and $t_{2g}$ should be at least 0.4 eV along the $\Gamma$-$X$ in the Brillouin zone. Though there are many unresolved issues, however, most experimental studies have been performed on NiO rather than MnO primarily because it is easier to grow in the single crystal form. To date, a few experiments that have probed the electronic structure of MnO have mostly relied on optical reflectance [16,17] and absorption methods [18], which have revealed a gap of 1.8 eV within the $3d$ band and an absorption edge of 3.8 eV. There are a few experimental papers [10,14,19] where the angle-integrated UPS spectra of a MnO(001) surface are shown for the PM insulating state of bulk MnO. There are also a few theoretical papers where the two-dimensional (2D) energy band dispersion of MnO are shown for the PM [20] and AFM [21] phases. To our knowledge, the study of the interfacial electronic structure and detailed two-dimensional band mapping of MnO(001) surfaces and ultrathin films below and above the Néel temperature are still missing in the literature. Moreover, the modifications to the electronic structure as a result of the magnetic phase transition (AFM to PM) is also not addressed till now.

Here we have investigated the thickness dependent electronic structure of MnO(001) films on Ag(001) substrate using XPS and ARPES measurements. We show that for lower film coverages some extra states arise in the electronic structure due to the substrate/interfacial effects, while from 6 ML onwards bulklike MnO(001) film has been realized. Our ARPES measurements show that the Mn-derived states ($e_g$ and $t_{2g}$) display a maximum relative dispersion of 1.2 eV between them, consistent with the theoretical calculations while contradicting the previous ARPES studies where a maximum dispersion of $\pm 0.1$ eV is reported. Overall our measured band dispersions also show good agreements with the theoretically calculated energy band dispersions. Furthermore, in order to understand the effects of magnetic phase transition on the electronic structure of MnO, we compare the valence electronic structure of PM and AFM phases. Band narrowing effects and sharpening of $^5e_g$ state

along with the band edge shift of 200 meV are observed during the transition from PM to AFM phase. These findings clearly show evidence of the decrease of $dd$ hopping integral during the magnetic phase transition (PM to AFM) as predicted by Terakura *et al.* [5] from band structure calculations. The presence of short-range antiferromagnetic correlations even in the PM phase of MnO is also evident from our valence band and core level photoemission data which have been discussed in the Sec. III D.

## II. EXPERIMENTAL DETAILS

Epitaxial MnO films were grown on Ag(001) single crystal substrate, prepared by standard cycles of Ar$^+$ ion sputtering (600 eV, 1 $\mu$A) for 15 min, followed by UHV annealing at 823 K for 30 min until a sharp (1 × 1) low energy electron diffraction (LEED) pattern was observed. The substrate preparation, growth, and LEED measurements were performed in the preparation chamber with a base pressure of 1 × 10$^{-10}$ mbar. High purity manganese (99.99%) was evaporated from a well-degassed water cooled $e$-beam evaporator at a constant rate of 0.4 Å/min, in an oxygen partial pressure of 2 × 10$^{-8}$ mbar, while the substrate was kept at room temperature (RT). After deposition, the film was annealed at 673 K in UHV for 10 min, then annealed at 473 K in the presence of oxygen for 10 min followed by further UHV annealing at 673 K for 10 min. The rate of Mn deposition was calibrated with a water-cooled quartz crystal thickness monitor, mounted on a linear drive which was moved to the sample position for rate measurements prior to deposition. The details of MnO growth optimization can be found from our previous work [22]. A monolayer (ML) of MnO is defined as an atomic density of 1.21 × 10$^{19}$ atoms/m$^2$, corresponding to that of the Ag(001) surface. The crystalline quality of the film was determined by a four-grid LEED apparatus (OCI Vacuum Microengineering) in the preparation chamber, while the XPS and ARPES measurements were performed *in situ* in the analysis chamber with a base pressure better than 8 × 10$^{-11}$ mbar and attached to the preparation (growth) chamber. ARPES experiments were performed using a combination of a VGScienta-R4000WAL electron energy analyzer with a 2D-CCD detector and a high flux Gammadata VUV He lamp attached with a VUV monochromator, which has been described in detail elsewhere [23]. We have used He I$_\alpha$(21.2 eV) and He II$_\alpha$(40.8 eV) resonance lines for the ARPES measurements, while the Al $K_\alpha$ monochromatic x-ray source (1486.6 eV) from VG SCIENTA was used for XPS measurements. The total experimental energy resolution for XPS and ARPES measurements was about 0.6 and 0.1 eV, respectively, including the thermal broadening near $E_F$ at room temperature. We have confirmed the absence of any charging effects on the MnO films (up to 10 ML) by varying the incident x-ray flux and observing no detectable binding energy shift or spectral shape changes of the core levels.

## III. EXPERIMENTAL RESULTS AND DISCUSSIONS

### A. Core level electronic structure

Evolution of the core level electronic structure of MnO with film thickness has been studied in order to probe the
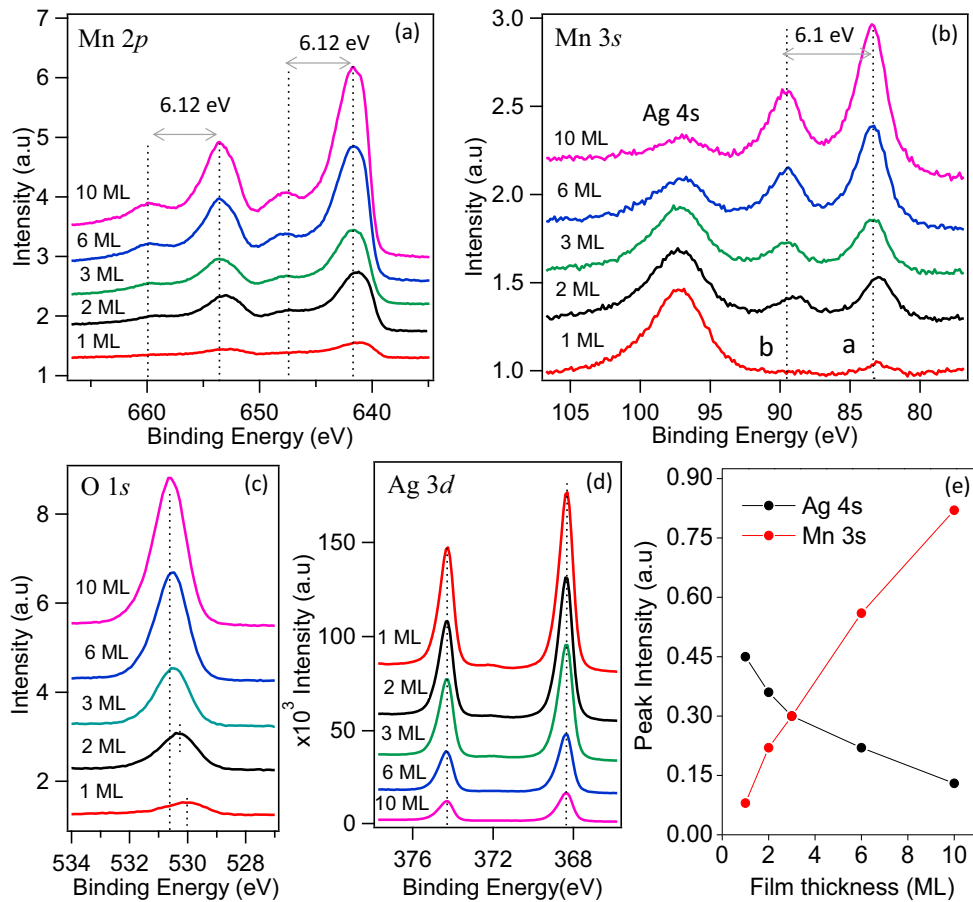
FIG. 1. (a) Mn $2p$ core level of MnO film for various film thickness. A charge transfer satellite peak is observed at a 6.12 eV higher binding energy position than the main peaks of Mn $2p$. (b) Mn $3s$ core level shows an exchange splitting of 6.10 eV. (c) and (d) O $1s$ and Ag $3d$ core level for different film thickness. (e) Intensity variation of the Mn $3s$ and Ag $4s$ peaks with film thickness.

chemical composition as well as to investigate the role of finite size effects (lower coordination number) and film-substrate interaction on the electronic structure. Thickness dependent evolution of Mn $2p$, Mn $3s$, O $1s$, and Ag $3d$ core levels are shown in Figs. 1(a)–1(d). Figure 1(a) shows with increasing film thickness that Mn $2p$ peaks are shifted towards the higher binding energy region up to 3 ML and beyond that no further peak shift is observed. The core level peak shifting in ultrathin films can be due to various factors such as the reduced dimensionality of the film (resulting from the reduced number of nearest neighbors), effect of the substrate induced strain, image charge screening effect on conducting substrate, etc. From our previous work [22], it is observed that there is a strain of 3.75% in going from 1 to 3 ML of the MnO film on Ag(001) substrate. However, in our estimation of the core level peak shifting based on the recent theoretical calculation [24] it is found that this effect may not be very significant (less than 30% of the observed shift). We believe that the significant effect is arising due to the presence of image charge screening at the metal/oxide interface, especially for the lower film coverages and may contribute significantly to the binding energy shift by lowering the effective $U$ at the interface. It is expected that the effects of image charge screening will decrease with increasing film coverages which will, in turn, increase the effective $U$ and binding energies to approach the bulk values. Similar core level

shifting for lower film coverages have already been reported for MgO films on Ag(001) substrates because of the image charge screening effects [1]. This has also been further established by a recent layer-resolved study of Auger transition from the MgO/Ag(001) ultrathin films [25]. The decrease of the effective $U$ for ultrathin layers is expected to decrease the electron correlation effects ($U/W$) in these materials, even though the bandwidth ($W$) also tends to decrease with film thickness. This is expected to decrease the correlation-induced band gap, which is also observed in our ARPES studies (see Sec. III B).

Furthermore, in the Mn $2p$ spectra, two charge transfer satellite peaks are observed along with the Mn $2p$ main peaks which are located at a 6.12 eV higher binding energy than the main peaks of the Mn $2p$. These findings are in good agreement with the Mn $2p$ core level spectra reported in the literature for the MnO(001) films [26]. A detailed description of the growth optimization of the MnO films on Ag(001) can be found in our previous work [22]. For low film coverages, the Mn $2p$ satellites are not properly visible, which can also be attributed to the reduced coordination resulting in the change of the multiplet structures. Figure 1(b) shows the XPS core level spectra of Mn $3s$ where a splitting of the Mn $3s$ level is observed due to the interaction of the spin in the Mn $3s$ level after photoemission and the resulting Mn $3d$ spin. With increasing film thickness, Mn $3s$ peaks are shifted towards higher binding
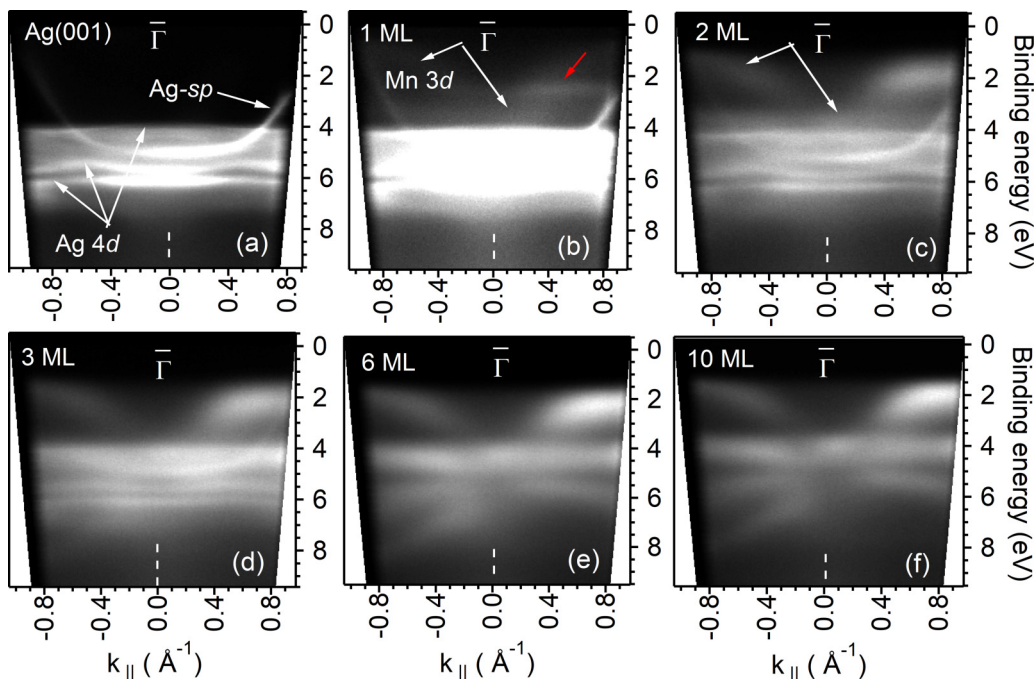
FIG. 2. Normal emission ARPES (around $\bar{\Gamma}$ along $\bar{\Gamma}$ to $\bar{X}$ direction) using He II$_\alpha$ light for different coverages of MnO(001) films on Ag(001) obtained at RT. Red arrow shows an extra interfacial band observed for the monolayer case.

energy, similar to Mn $2p$ spectra, while no further peak shift is observed from 3 ML onwards. For 1 ML coverage, a very weak Mn $3s$ signal is observed due to the small amount of material, still, the main peak can be observed. In Fig. 1(b), "a" and "b" are the Mn $3s$ spin split state and the corresponding electron configuration of the states are $3d \uparrow\uparrow\uparrow\uparrow\uparrow 3s \uparrow$ and $3d \uparrow\uparrow\uparrow\uparrow\uparrow 3s \downarrow$, respectively. The theoretically calculated value of this splitting for MnO is ∼6.15 eV [27], which is a close match with our experimental value of 6.10 eV. Figure 1(c) shows the O $1s$ core level spectra of the MnO films. Similar to the case of Mn $2p$ and Mn $3s$, the O $1s$ peak is also shifted towards the higher binding energy with increasing film thickness resulting from the increased nearest-neighbor coordination as well as from the reduced charge screening effects (or increased electron correlation effects). Figure 1(d) shows the Ag $3d$ core level spectra for the underlying Ag(001) substrate. With increasing MnO film thickness, the Ag $3d$ peaks does not shift in energy position indicating that there is no alloying between Mn and Ag at the interface.

Furthermore, some understanding of the possible growth mode can be made from the intensity variation of the core lines of the substrate and the adsorbate atoms by measuring as a function of the coverage. In order to get an idea about the possible growth mode, the intensity variation of the Mn $3s$ and Ag $4s$ peaks with the film thickness are shown in Fig. 1(e). With increasing film thickness, the intensity of the Mn $3s$ increases while that of Ag $4s$ decreases and these two curves intersect each other at a critical film thickness of ∼3 ML. It is known that the measured XPS intensity ($I$) depends on the mean-free path ($\lambda$) of the electrons of a particular energy and on the amount of matter which has to be penetrated. Thus, by taking simple continuum-type description the variation of the core level intensity for substrate (adsorbate) should expect an exponential-like decay (increase) as the change of the XPS line

intensity "$dl$" is related to the change "$dh$" in film thickness by $dl/I = -dh/\lambda$. Thus, this type of intensity variation curves [see Fig. 1(e)] demonstrate a clear signature of the layer-by-layer growth mode rather than an island growth mode [28]. For island type growth, large areas of the substrate remain free from the adsorbent, thus the substrate signals should be much less suppressed than in the case of layer-by-layer growth with complete overlayers. Only a slow increase and decrease of the film and of the substrate signal, respectively, will be observed with the coverage. In our experiment, rapid increase and decrease of the film and substrate core level intensities with a crossing point at lower film coverage are clear evidence of the layer-by-layer growth of the MnO film.

## B. Valence band structure of MnO/Ag(001): Thickness dependence

In case of bulk MnO, it is known that the occupied Mn $3d$ bands are mainly located between the Fermi level and 4.0 eV below it, while the O $2p$ bands are located between 4 and 9 eV. More recent calculations show that the Mn $3d$ and O $2p$ states contribute to the overall valence band but with different weights [20]. The experimental valence band electronic structure of MnO films for different film thicknesses on Ag(001) substrate are shown in Fig. 2, where He II$_\alpha$ ($h\nu = 40.8$ eV) was used as the excitation source. The $sp$ bands of Ag have much lower intensity compared to the Ag $4d$ bands and the Mn $3d$ bands fall in the energy range of the Ag-$sp$ bands which enable the Mn $3d$ bands to be easily detectable from the very initial stages of the growth [see Fig. 2(b)]. However, the O $2p$ bands cannot be distinguished clearly before the film coverage of 6 ML due to the overlapping with the Ag $4d$ bands which mask the MnO features, especially for very low film coverages. From 6 ML onwards, the $4d$ band features of the Ag
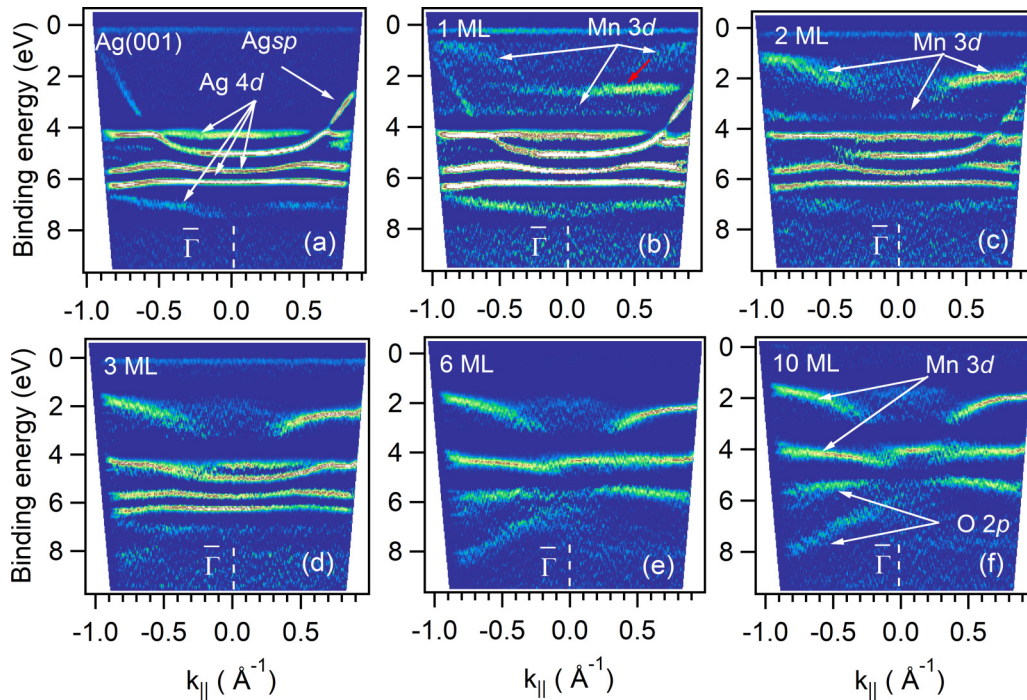
FIG. 3. The second derivative of the ARPES data shown in Fig. 2 using He II$_\alpha$ light for different coverages of MnO(001) films at RT. The second derivative images were obtained using the method suggested by Zhang *et al.* [29].

substrate are almost completely suppressed and only the bands from MnO(001) film are visible. For better visualization of the bands, the second derivative of the ARPES data is presented in Fig. 3 for different MnO film thickness. A flat bandlike feature observed just below the Fermi level [see Figs. 3(a)–3(d)] is, in fact, an artifact of the second derivative processing and resulting from the presence of the Fermi edge of Ag(001) observed up to 3 ML MnO coverage. From Fig. 3(b) it is clear that the valence band (VB) maximum is located at 0.7 eV and with increasing film coverage it is shifted towards the higher binding energy position and from 3 ML onwards it is fixed at around 2.0 eV. So with increasing film thickness, the MnO film becomes more insulating with its band gap approaching bulk MnO, due to the increased atomic coordination as well as electron correlation effects. Similar binding energy shifts have also been observed for the core levels of MnO as discussed in the previous section. We have also performed detailed surface magnetic characterization of the films with film thickness, further evidencing the reduced effective $U$ value for lower film coverages and will be the subject of a future article [30]. Furthermore, for the 1 ML coverage film, a new flat band is clearly visible at 2.5 eV [indicated by red arrow in Fig. 3(b)] which is not visible for other film coverages. This flat band, observed for the monolayer case, is most likely to be a manifestation of the interfacial states arising due to the film-substrate interaction. Similar, flat interfacial bands have also been observed for low coverages of NiO [31] and CoO [32] films. One more additional band is visible at 3.4 and 3.7 eV binding energy for 1 and 2 ML coverages, respectively, and is absent from films of higher coverages. We realize this band is actually the Mn-$t_{2g}$ band and with increasing film thickness it shifts towards higher binding energy and ultimately moves to the bulk Mn-$t_{2g}$ band position for higher film coverages. In

order to identify these states more clearly, we have presented the energy distribution curves (EDCs) at $\bar{\Gamma}$ in Fig. 4(a) for different MnO coverage. It is also to be noted that the features of the peaks in Figs. 4(a) and 4(b) appear broader than the raw data shown in Fig. 2 as the EDCs are shown with angular averaging over $\pm 10$ deg polar angle around $\bar{\Gamma}$ point. In Fig. 4(a) the states labeled by "a" and "b" represents the $e_g$ and $t_{2g}$ states of MnO. Evolution of these states and interfacial state/band with film thickness are indicated by the vertical lines. For lower
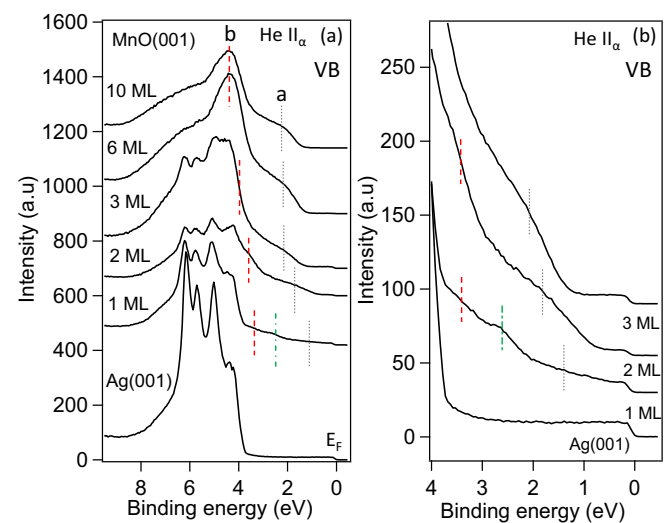


FIG. 4. (a) EDC plot around $\bar{\Gamma}$ for the various film thickness of MnO on Ag(001) measured at RT using He II$_\alpha$ photons. EDCs are shown with angular averaging over $\pm 10$ deg polar angle around $\bar{\Gamma}$ point. (b) Zoomed-in view of the same spectra near the Fermi level. Position of the Mn 3$d$ bands are indicated by vertical lines.

film coverages, the intensity of these states are very weak, so a zoomed-in view of the same spectra near the Fermi level is shown in Fig. 4(b), where these states can be clearly visible. The signature of the Fermi edge from the underlying Ag(001) substrate can be clearly visible in Fig. 4(b) up to 3 ML coverage of MnO. Peak "a" ($e_g$ states, dotted lines) is found shifting towards higher binding energy with increasing film thickness and is fixed at 2.3 eV from 3 ML onwards. Peak "b" ($t_{2g}$ states, dashed lines) also shifts to higher binding energy and is fixed at 4.3 eV beyond 6 ML coverages. The vertical (dot-dashed) line at 2.5 eV represents the interfacial state/band for the monolayer coverage, as discussed earlier. From 6 ML onwards, the EDC looks similar to the previously reported EDCs [15] as well as the UPS spectra [10,19,33] of the MnO(001) single crystal surfaces.

## C. Band dispersions along $\bar{\Gamma}$-$\bar{X}$ and $\bar{\Gamma}$-$\bar{M}$: 10 ML MnO/Ag(001)

ARPES is a well-established experimental technique that has been used to determine the energy band dispersions of many materials including metals, semiconductors, metal oxides, and intermetallics. However, very few angle-resolved measurements have been performed on transition-metal oxide single crystals since most of the oxide materials are highly insulating leading to charging issues. Another common issue is the lack of cleavage planes in these oxide single crystals, making the *in situ* preparation of surfaces a daunting task. However, both these problems can be overcome by depositing a thin film of the oxide material epitaxially on a suitable metallic substrate. In Figs. 5(a) and 5(b) the valence band electronic structure of a 10 ML MnO film along the $\bar{\Gamma}$-$\bar{X}$ direction of the MnO(001) surface Brillouin zone (SBZ) are shown for He I$_\alpha$ ($h\nu = 21.2$ eV) and He II$_\alpha$ ($h\nu = 40.8$ eV) photons, respectively. Figures 5(c) and 5(d) show their respective second derivative images which enable us to clearly determine the band dispersions. Figures 5(e) and 5(f) are the electronic band structure along the $\bar{\Gamma}$-$\bar{M}$ direction of the MnO(001) SBZ and its derivative image, respectively. The ultraviolet photons, with their limited mean-free paths of the photoemitted electrons, are unable to probe the substrate Ag bands that reside below the 10 ML MnO film. Hence, the experimental ARPES spectrum can be directly compared to the theoretically calculated band structure for bulk MnO. Our experimental band dispersions along the $\bar{\Gamma}$-$\bar{M}$ [see Figs. 5(e) and 5(f)] are quite similar to the theoretical band dispersions for bulk MnO along [100] direction, i.e., along $\Gamma$-$X$ direction [20]. Because by changing the $k_\parallel$ along the $\bar{\Gamma}$-$\bar{M}$ direction of the MnO(001) SBZ, we are actually mapping out the electronic states along the $\Gamma$-$\Delta$-$X$ symmetry direction of the bulk Brillouin zone (BBZ). On the other hand, $\bar{\Gamma}$-$\bar{X}$ data also show good agreement with the calculated surface band structures of MnO(001) [21]. A clear dispersion of the $e_g$ states relative to the $t_{2g}$ states are seen along both symmetry directions. A previously reported ARPES study [15] suggested that these Mn-derived ($e_g$ and $t_{2g}$) states are separated by 1.8 eV and do not disperse by more than $\pm 0.1$ eV with respect to each other across the entire Brillouin zone. They explain the observed lack of dispersion as a strong evidence for localized $3d$ electrons. However, their results contradict with our measured relative dispersion between $e_g$ and $t_{2g}$ states of about 1.2 eV (along $\bar{\Gamma}$ to $\bar{M}$ direction) as
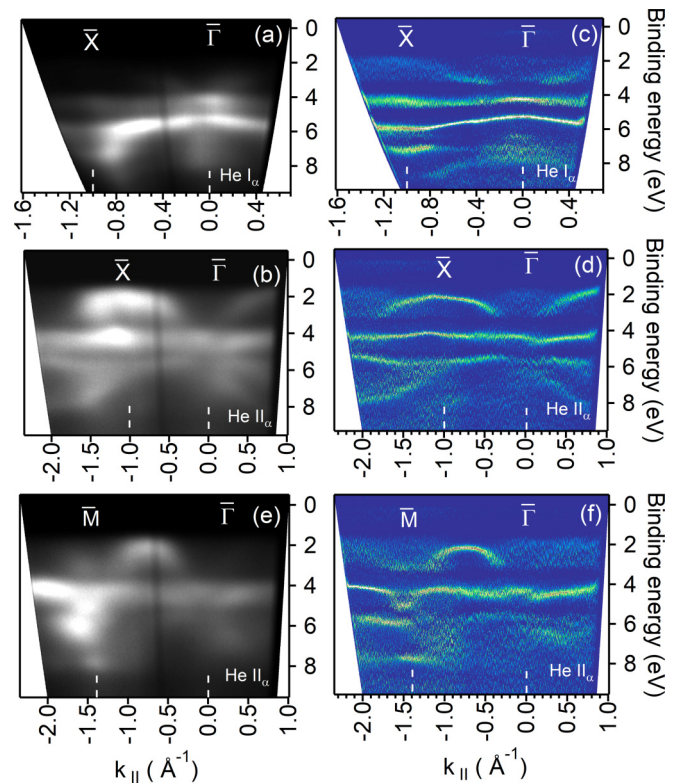


FIG. 5. (a) and (b) ARPES for 10 ML MnO/Ag(001) along $\bar{\Gamma}$-$\bar{X}$ direction of the MnO(001) SBZ using He I$_\alpha$ and He II$_\alpha$. (c) and (d) The second derivatives of (a) and (b). (e) ARPES data along $\bar{\Gamma}$-$\bar{M}$ direction using He II$_\alpha$ and (f) second derivative of "e."

well as with the band structure calculations. The calculated band structure results [34,35] predicted a relative dispersion between $e_g$ and $t_{2g}$ for MnO which is at least 0.4 eV along $\Gamma$-$X$. In order to search for the origin of the dispersions, we look at the calculated partial density of state (PDOS) for MnO [20]. According to these calculations [20], the O $2p$ states are located between 9 and 1.5 eV with different spectral weights and the lower Hubbard band, which consists of the respective Mn-$3d$ $t_{2g}$ and $e_g$ states, contributions at 4 and 2.3 eV, respectively. Furthermore, the Zhang-Rice band, the bound state that appears when a strongly interacting band is hybridized with the charge reservoir, can be seen as a peak at 1.5 eV in O $2p$ states together with Mn $3d$ $e_g$ states. If we look at our experimental band dispersion [see Figs. 5(a)–5(f)], the band at 4 eV is almost nondispersive but the band at ~2.3 eV has some dispersions in the $\bar{\Gamma}$-$\bar{X}$ and $\bar{\Gamma}$-$\bar{M}$ directions (see Fig. 5). The agreement between our experiments and the calculations gives the confidence that our measured band dispersions are accurate and the observed dispersions of the Mn $3d$ states are due to hybridization between Mn $3d$ $e_g$ and O $2p$ states because of the dispersive nature of the O $2p$ bands.

It should be noted that in the previous ARPES study [15], they mention that they were unable to do detailed band mapping of the states within the Brillouin zone between 1 and 5 eV due to the broad and complex nature of the peaks. This, together with the absence of dispersions of the Mn-$3d$ $t_{2g}$ and $e_g$ states indicate that sample charging effects were responsible for their strange observations. In fact, in the experimental

section of Ref. [15], they clearly mention that the MnO crystals used had high bulk resistivity and could only observe diffused $(1 \times 1)$ LEED pattern for high incident electron energies (>250 eV). Even during photoemission, they have reportedly observed steady-state charging, which prevented a precise determination of the Fermi level as well as resulted in the observation of broad bands. Moreover, their single crystal was not a single phase and reportedly contained some $\alpha$-Mn$_3$O$_4$ impurity phases. Thus, our present work shows the importance of studying well characterized epitaxial thin films of insulating oxide materials grown on metallic substrates, for a precise determination of their electronic structures.

Furthermore, the dependence of the photoemission cross section on the electronic structure of MnO is also clearly visible from our experimental data presented in Figs. 5(a)– 5(d). The O $2p$ bands are clearly visible when probed by He I$_\alpha$ photons while Mn $3d$ bands are clearly visible when probed by the He II$_\alpha$ photons. For example, at $\bar{\Gamma}$, O $2p$ bands around the 8 eV binding energy region is only visible with He I$_\alpha$. Thus, He I$_\alpha$ photons are more suitable to probe the O $2p$ bands while He II$_\alpha$ photons are more suitable for the Mn $3d$ bands. We have estimated the ratio of the photoemission cross sections (Mn $3d$/O $2p$) from our ARPES data by taking the intensity ratio of Mn $3d$/O $2p$ bands and it is found to be around 1.31 and 0.52 for 40.8 and 21.2 eV photon energies, respectively, which are in good agreement with the theoretical values of 1.23 and 0.5 reported in Ref. [36]. It is also important to note that in the ARPES measurements of MnO(001) surface, by changing the photon energy from He I$_\alpha$ to He II$_\alpha$, we are probing different cuts of the $k$ space ($k_\perp$) along the [001] direction. Thus, it is expected to show $k_\perp$ dispersions for He I$_\alpha$ and He II$_\alpha$ photon energies for the 10 ML MnO film. It is observed that at $\bar{\Gamma}$ the bands at 2.3 eV ($e_g$) and 4.3 eV ($t_{2g}$) for He II$_\alpha$ are shifted towards higher binding energies by 0.4 and 0.2 eV for He I$_\alpha$, indicating the $k_\perp$ dependence of the Mn $3d$ $e_g$ and $t_{2g}$ bands. The observed $k_\perp$ dispersions are also found to be in good agreement with the reported theoretical band dispersions [20], where weak dispersions along $\Gamma$-$X$ can be seen.

### D. Electronic structure of MnO film: PM vs AFM phase

Though it is well known that the electronic structure is directly related to the magnetism, its experimental evidence is missing for most of the transition metal oxides. Here, in order to understand the effect of magnetic transition on the electronic structure of MnO, we have measured the valence band electronic structure in both PM and AFM phases. Figures 6(a) and 6(b) show the valence band electronic structure of 10 ML MnO(001) film grown on Ag(001) around $\bar{\Gamma}$ at RT (PM phase) and 108 K (AFM phase), respectively. Both ARPES images using He II$_\alpha$ photons show similar dispersions and no noticeable changes have been visualized between them. However, the EDCs at $\bar{\Gamma}$ [see Fig. 6(c)] show some changes in the spectral features across the magnetic phase transition. Figures 6(d) and 6(e) show the LEED pattern of 10 ML MnO(001) film taken for the sample temperatures of 300 and 108 K, respectively. The half-integer order spots [e.g., (1/2, 0)] are visible at 108 K [see Fig. 6(e)], while no such spots are observed at 300 K [see Fig. 6(d)]. These half-integer order spots are originating from the coherent exchange scattering of

the incident electrons by the antiferromagnetically ordered surface Mn moments, similar to the case of NiO [37,38]. Moreover, the presence of long-range magnetic ordering transition (PM-AFM) with surface Néel temperature of about 145 K is confirmed on the MnO film from our LEED studies using the temperature-dependent intensity measurements of the half-integer order spots which is shown in Fig. 6(f). Detailed magnetic characterization of the sample can be found in Ref. [30]. Thus, we can associate the observed changes in Fig. 6(c) to be originating from the PM-AFM transition. In Fig. 6(c) we have labeled different peaks of the spectra as a, b, c, d, and e, respectively. The origin of these peaks has been well understood on the basis of the ligand field theory combined with configuration-interaction (CI) cluster approach [19]. The photoemission initial state of Mn$^{2+}$ ($3d^5$) ion has $^6A_{1g}$ symmetry and after removing one $3d$ electron from $t_{2g}$ or $e_g$, the photoemission final state becomes $^5t_{2g}$ and $^5e_g$ symmetry. But the real final state of the system is more complex because of the presence of $d^6\underline{L}$ initial state (due to the transfer of the sixth $d$ electron from ligand to the Mn$^{2+}$ ion) which is mixed to the ground state and after photoionization of the sixth $d$ electron, leaving behind a $d^5\underline{L}$ final state which has $^7t_{2g}$ and $^7e_g$ symmetry states. Thus, the real final state is a mixture of Mn $3d$-hole and O $2p$-hole ($d^4$-$d^5\underline{L}$) states, so in addition to the $^5t_{2g}$ and $^5e_g$ final states, there are also $^7t_{2g}$ and $^7e_g$ states. The peaks a and b in Fig. 6(c) arise mainly from the $^5e_g$ and $^5t_{2g}$ states while hybridization with the O $2p$ states is still present. Peaks c and d arise due to the hybridization of O $2p$ with the $^7t_{2g}$ and $^7e_g$ states. The origin of peak e is reported to be controversial in the literature with some suggesting that it is related to the defect states [10,33], while the calculations based on CI suggest that it is an intrinsic feature of the MnO [19]. However, our valence band data does not show any significant amount of defect states near the Fermi level [see Fig. 6(c)], unlike the case of NiO thin films [39,40]. Thus, in the grown MnO film, the appearance of state e without the presence of defect states in the valence band near $E_F$ supports the intrinsic origin of this feature.

In the inset of Fig. 6(c), the zoomed-in view of the spectra near the Fermi level is shown where the valence band edge shifts to higher binding energy by ~200 meV for the AFM phase in comparison to the PM phase. This energy shift demonstrates that the AFM phase is more insulating than the PM phase, resulting from the long-range magnetic ordering. It is also observed from Fig. 6(c) that in the AFM phase, the $^5e_g$ symmetry state (peak 'a') is more intense as well as narrower than that in the PM phase. These results are in contradiction with the previously reported temperature dependent valence band photoemission data by Hermsmeier *et al.* [14]. Their results show, below the Néel temperature (AFM phase), the valence band gets broader than PM phase and the valence band edge shifts towards the lower binding energy which is exactly the opposite to our results. We believe these studies failed to pick up the changes in the valence band across the Néel temperature due to the huge charging effects observed on the polished single crystal of MnO(001) [14]. However, our observation of band narrowing and sharpening of the $^5e_g$ state in the AFM phase is consistent with the band structure calculation for the AFM-II phase of MnO using the augmented spherical wave (ASW) method by Terakura *et al.*
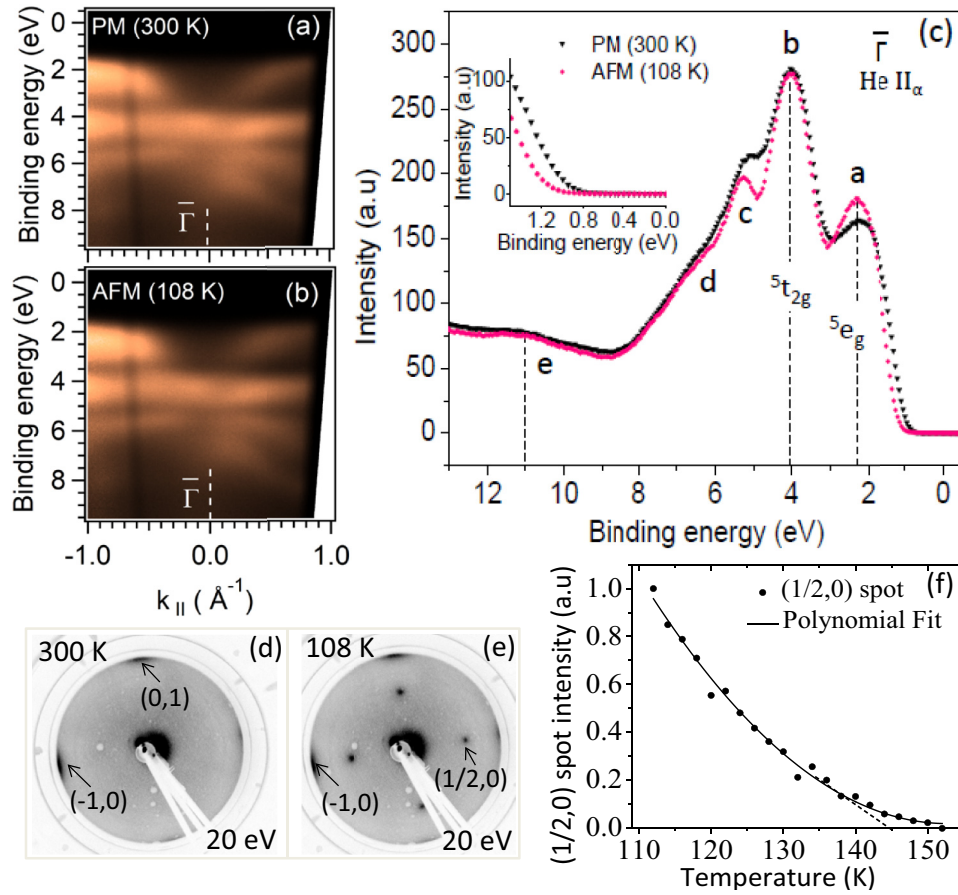
FIG. 6. ARPES at $\bar{\Gamma}$ (along $\bar{\Gamma}$ to $\bar{X}$) of 10 ML MnO film using He II$_\alpha$ photons for (a) PM (300 K) and (b) AFM (108 K) phases. (c) ARPES EDC plot around $\bar{\Gamma}$ for PM and AFM phases. Inset shows the zoomed-in view of the spectra near the Fermi level. (d) and (e) LEED pattern of 10 ML MnO film for the sample temperature of 300 and 108 K, respectively, with an electron beam energy of 20 eV. First order diffraction spots are just out of the field-of-view due to the low energy of the electron beam. (f) Intensity variation of the (1/2, 0) spot with respect to temperature is fitted with a polynomial.

[5]. Experimentally, the existence of the AFM-II phase of MnO has already been confirmed by neutron diffraction and spin-polarized photoelectron diffraction (SPPD) experiments [41–43] as well as by our recent LEED experiments [30]. Terakura *et al.* [5] have also predicted that the change in the $dd$ hopping during the magnetic phase transition as the origin of the sharpening of $^5e_g$ state as well as the gap opening in the AFM phase. The spectral weight and width of the $^5t_{2g}$ and $^5e_g$ peaks are determined by the $dd$ hopping between the first-nearest-neighbor cations and the second-nearest-neighbor cations, respectively [6]. Thus in the AFM phase, the observed enhancement of the $^5e_g$ peak intensity and the band narrowing effects are the consequence of the decrease of the effective $dd$ hopping (i.e., reduced orbital overlap) between the second-nearest-neighbor cations. As in the AFM-II phase of MnO, the magnetization varies in the [111] direction, thus the coupling between the oppositely magnetized cation atoms (second-nearest-neighbor cations) is mediated via the intermediate oxygen $p$ orbital which decreases the effective $dd$ hopping due to the $dd\sigma$ type interaction, resulting in the narrowing of the $e_g$ band. No change in the $t_{2g}$ spectral features is observed during the magnetic phase transition [see Fig. 6(c)] as the $t_{2g}$ spectral weight is determined by the first-nearest-neighbor interaction

between cations, which does not get affected by the magnetic ordering. The feature c also show some changes upon the magnetic phase transition as it contains $^7e_g$ component, which can also be seen from the theoretical calculations [6].

Furthermore, the temperature dependence of the core level photoemission was also studied for the PM and AFM phases of MnO. Figures 7(a) and 7(b) show the Mn $2p$ and Mn $3s$ core levels for 300 (PM) and 108 K (AFM) phases of 10 ML MnO film. The Mn $2p_{3/2}$ peak shows multiplet structures arising due to the local and nonlocal screening effects [27,44], labeled as "A" and "B," respectively. Peak A is associated with the local charge transfer screening within the core-excited MnO$_6$ octahedron, while peak B is due to the nonlocal screening accompanied by a Zhang-Rice doublet formation [45,46]. The Mn $2p_{3/2}$ core level shows similar spectral features across the magnetic phase transition, although some changes can be observed in the multiplet features. However, the core level features of Mn $3s$ are quite similar in both magnetic states [see Fig. 7(b)]. It is clear from the inset of Fig. 7(a) that during PM to AFM phase transition, the nonlocal component (B) of the Mn $2p_{3/2}$ core level is shifted towards lower binding energy side by 150 meV, while the local component (A) does not change its position, yielding a slightly larger splitting between them for the AFM
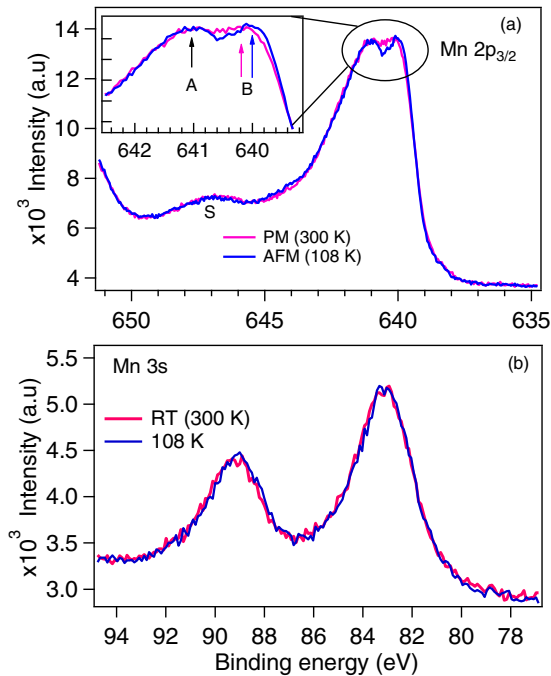
FIG. 7. (a) Mn $2p_{3/2}$ and (b) Mn $3s$ core level spectra collected with a photon energy of 1486.6 eV for both AFM and PM phases at sample temperatures of 108 K and RT (300 K), respectively. "S" denotes the satellite peak of Mn $2p_{3/2}$. "A" and "B" peaks originating from the local and nonlocal screening effects. Position of the "B" peak is shifted towards the lower binding energy position for the AFM case.

phase. Moreover in the AFM phase, "A" and "B" are well resolved and a small increase in the "B" intensity with respect to "A" can be observed. Similar to our results, well-resolved local and nonlocal screening features have also been reported for the AFM phase of NiO, while it is indistinct for the PM phase [45,47]. They have also shown that the double peaks "A" and "B" are well reproduced in their AFM calculation, while for the PM phase these features are not clearly separated. These calculations have demonstrated that the hybridization between Mn $3d$ states with the rest of the crystal shows strong spin dependence in the AFM phase and plays a crucial role in the formation of the fine structures of the $2p$ core levels [45,47]. Moreover, strong dependence of the line shape of Mn $2p$ and Fe $2p$ on the magnetic state has been reported for the different manganites [46,48] and FeRh [49] systems, respectively.

Even though we have observed small changes in both valence band and Mn $2p$ core level across the magnetic phase transition, it should be pointed out that these changes are still not as significant as expected. This is likely to be due to the presence of short-range antiferromagnetic domain ordering in MnO even above its Néel temperature. The presence of short-range antiferromagnetic ordering for bulk MnO is already confirmed by neutron diffraction and SPPD experiments [41–43]. Moreover, a transition from this short-range ordered state to the PM state with $T_{SR} \approx 4.5T_N$ is also observed by the SPPD experiments [14]. The existence of short-range antiferromagnetic correlations even well into the PM phase of MnO with correlation lengths larger than the photoemission correlation lengths are likely responsible for

their similar electronic structures and deserve further detailed investigations. However, LEED with its larger coherence lengths (of few hundred angstroms), is not sensitive to these short-range antiferromagnetic correlations and detects only the long-range antiferromagnetic ordering at the surfaces.

## IV. CONCLUSION

In summary, a detailed thickness and temperature dependent study of the electronic structure of ultrathin MnO(001) film on Ag(001) has been investigated using XPS and ARPES techniques. Our XPS measurements together with a growth optimization study [22] have confirmed the layer-by-layer growth mode of the film with MnO stoichiometry and structure. For low film coverages (<3 ML), we find some new states arising in the valence band due to the substrate/interfacial effects, while from 6 ML onwards bulklike MnO(001) film is realized. We have compared the experimental band dispersions obtained from ARPES with the available calculations and find good agreements between them. Detailed band mapping along the $\bar{\Gamma}$-$\bar{X}$ and $\bar{\Gamma}$-$\bar{M}$ directions of the MnO(001) films reveal up to 1.2 eV relative dispersion between the Mn-derived $e_g$ and $t_{2g}$ states. This observation is in contradiction with the earlier experimental results performed on single crystal MnO(001) surface where a maximum relative dispersion of $\pm 0.1$ eV was obtained, indicating the importance of studying these insulating materials devoid of charging effects. Moreover, our results are an excellent match with the theoretically predicted dispersions where a dispersion of about 0.4 eV is evident along the $\bar{\Gamma}$-$\bar{X}$ direction. Hybridization between O $2p$ and Mn $e_g$ states are responsible for the observed dispersions, resulting from the highly dispersive nature of the O $2p$ bands. Our temperature dependent valence band studies for the PM and AFM phases of MnO(001) thin films confirm the band narrowing effects and sharper $^5e_g$ states for the AFM phase than the PM phase, in agreement with the previous theoretical predictions by Terakura *et al.* [5]. The decrease of the effective $dd$ hopping resulting from the $dd\sigma$ type interaction between oppositely magnetized cation atoms (second-nearest-neighbor cations) are likely to be the origin of these effects. Mn $2p$ core level measurements for the AFM phase also show that the AFM ordering plays a crucial role in the details of the multiplet structures of the system. Furthermore, the changes in the effective $dd$ hopping up on PM to AFM transition should also be applicable to other prototype materials such as CoO, NiO, etc. and are expected to show similar changes in their spectral features, like MnO. However, the lack of significant changes in the valence band electronic structure across the AFM-PM phase transition of MnO are attributed to the existence of short-range AFM correlations even deep inside the PM phase, which need to be explored further. Our present work shows the importance of studying well characterized epitaxial thin films of insulating oxide materials grown on metallic substrates, for a precise determination of their electronic structures.

[1] S. Altieri, L. Tjeng, and G. Sawatzky, Thin Solid Films **400**, 9 (2001).

[2] H. Ohldag, A. Scholl, F. Nolting, E. Arenholz, S. Maat, A. T. Young, M. Carey, and J. Stöhr, Phys. Rev. Lett. **91**, 017203 (2003).

[3] J. E. Pask, D. J. Singh, I. I. Mazin, C. S. Hellberg, and J. Kortus, Phys. Rev. B **64**, 024403 (2001).

[4] J. Hubbard, Proc. R. Soc. London Ser. A **281**, 401 (1964).

[5] K. Terakura, T. Oguchi, A. R. Williams, and J. Kübler, Phys. Rev. B **30**, 4734 (1984).

[6] E. J. Ojala and K. Terakura, Phys. Rev. B **33**, 2733 (1986).

[7] M. Belkhir and J. Hugel, Solid State Commun. **70**, 471 (1989).

[8] J. Hugel and M. Belkhir, Z. Phys. B: Condens. Matter **79**, 57 (1990).

[9] I. A. Drabkin, L. T. Emel'yanova, R. N. Iskenderov, and Y. M. Ksendzov, Fiz. Tverd. Tela (Leningrad) **10**, 3082 (1968) [Sov. Phys. Solid State **10**, 2428 (1969)].

[10] A. Fujimori, N. Kimizuka, T. Akahane, T. Chiba, S. Kimura, F. Minami, K. Siratori, M. Taniguchi, S. Ogawa, and S. Suga, Phys. Rev. B **42**, 7580 (1990).

[11] A. Fujimori, N. Kimizuka, M. Taniguchi, and S. Suga, Phys. Rev. B **36**, 6691 (1987).

[12] S. Shin, S. Suga, M. Taniguchi, M. Fujisawa, H. Kanzaki, A. Fujimori, H. Daimon, Y. Ueda, K. Kosuge, and S. Kachi, Phys. Rev. B **41**, 4993 (1990).

[13] A. Fujimori, *Core-Level Spectroscopy in Condensed Systems*, Springer Series in Solid-State Sciences, edited by J. Kanamori and A. Kotani (Springer, Berlin, Heidelberg, 1988), Vol. 81, pp. 136–145.

[14] B. Hermsmeier, J. Osterwalder, D. J. Friedman, B. Sinkovic, T. Tran, and C. S. Fadley, Phys. Rev. B **42**, 11895 (1990).

[15] R. J. Lad and V. E. Henrich, Phys. Rev. B **38**, 10860 (1988).

[16] L. Messick, W. Walker, and R. Glosser, Surf. Sci. **37**, 267 (1973).

[17] Y. M. Ksendzov, I. L. Korobough, and K. K. Sidorin, and G. P. Startsev, Sov. Phys. (Solid State) **18**, 99 (1976).

[18] D. R. Huffman, R. Wild, and M. Shinmei, J. Chem. Phys. **50**, 4092 (1969).

[19] J. Van Elp, R. H. Potze, H. Eskes, R. Berger, and G. A. Sawatzky, Phys. Rev. B **44**, 1530 (1991).

[20] I. Nekrasov, N. Pavlov, and M. Sadovskii, J. Exp. Theor. Phys. **116**, 620 (2013).

[21] A. Schrön, M. Granovskij, and F. Bechstedt, J. Phys.: Condens. Matter **25**, 094006 (2013).

[22] A. K. Kundu and K. S. Menon, J. Cryst. Growth **446**, 85 (2016).

[23] S. K. Mahatha and K. S. R. Menon, Curr. Sci. **98**, 759 (2010).

[24] F. Shayeganfar, K. S. Vasu, R. R. Nair, F. M. Peeters, and M. Neek-Amal, Phys. Rev. B **95**, 144109 (2017).

[25] T. Jaouen, S. Tricot, G. Delhaye, B. Lépine, D. Sébilleau, G. Jézéquel, and P. Schieffer, Phys. Rev. Lett. **111**, 027601 (2013).

[26] M. Langell, C. Hutchings, G. Carson, and M. Nassir, J. Vac. Sci. Technol. A **14**, 1656 (1996).

[27] F. Müller, R. De Masi, D. Reinicke, P. Steiner, S. Hüfner, and K. Stöwe, Surf. Sci. **520**, 158 (2002).

[28] H. Lüth, *Solid Surfaces, Interfaces and Thin Films*, Vol. 4 (Springer, Berlin, 2001).

[29] P. Zhang, P. Richard, T. Qian, Y.-M. Xu, X. Dai, and H. Ding, Rev. Sci. Instrum. **82**, 043712 (2011).

[30] A. K. Kundu and K. S. R. Menon (unpublished).

[31] J. Das and K. S. Menon, J. Electron Spectrosc. Relat. Phenom. **203**, 71 (2015).

[32] S. Barman and K. S. R. Menon (unpublished).

[33] M. Nagel, I. Biswas, P. Nagel, E. Pellegrin, S. Schuppler, H. Peisert, and T. Chassé, Phys. Rev. B **75**, 195426 (2007).

[34] T. M. Wilson, J. Appl. Phys. **40**, 1588 (1969).

[35] O. Andersen, H. L. Skriver, H. Nohl, and B. Johansson, Pure Appl. Chem. **52**, 93 (1980).

[36] J. Yeh and I. Lindau, At. Data Nucl. Data Tables **32**, 1 (1985).

[37] K. S. R. Menon, S. Mandal, J. Das, T. O. Menteş, M. A. Niño, A. Locatelli, and R. Belkhou, Phys. Rev. B **84**, 132402 (2011).

[38] P. Palmberg, R. DeWames, and L. Vredevoe, Phys. Rev. Lett. **21**, 682 (1968).

[39] J. Das and K. S. Menon, Appl. Surf. Sci. **359**, 61 (2015).

[40] F. Reinert, P. Steiner, S. Hüfner, H. Schmitt, J. Fink, M. Knupfer, P. Sandl, and E. Bertel, Z. Phys. B: Condens. Matter **97**, 83 (1995).

[41] B. Hermsmeier, J. Osterwalder, D. J. Friedman, and C. S. Fadley, Phys. Rev. Lett. **62**, 478 (1989).

[42] A. Renninger, S. Moss, and B. Averbach, Phys. Rev. **147**, 418 (1966).

[43] Z.-X. Shen, J. Allen, P. Lindberg, D. Dessau, B. Wells, A. Borg, W. Ellis, J. Kang, S.-J. Oh, I. Lindau *et al.*, Phys. Rev. B **42**, 1817 (1990).

[44] F. De Groot and A. Kotani, *Core Level Spectroscopy of Solids* (CRC, Boca Raton, FL, 2008).

[45] A. Hariki, Y. Ichinozuka, and T. Uozumi, J. Phys. Soc. Jpn. **82**, 043710 (2013).

[46] K. Horiba, M. Taguchi, A. Chainani, Y. Takata, E. Ikenaga, D. Miwa, Y. Nishino, K. Tamasaku, M. Awaji, A. Takeuchi *et al.*, Phys. Rev. Lett. **93**, 236401 (2004).

[47] A. Hariki, T. Uozumi, and J. Kuneš, Phys. Rev. B **96**, 045111 (2017).

[48] M. van Veenendaal, Phys. Rev. B **74**, 085118 (2006).

[49] A. Gray, D. Cooke, P. Krüger, C. Bordel, A. Kaiser, S. Moyerman, E. Fullerton, S. Ueda, Y. Yamashita, A. Gloskovskii *et al.*, Phys. Rev. Lett. **108**, 257208 (2012).